

## Modeling Optical Turbulence and Seeing over Mauna Kea: Verification and Algorithm Refinement\*

T. CHERUBINI, S. BUSINGER, AND R. LYMAN

*University of Hawaii at Manoa, Honolulu, Hawaii*

(Manuscript received 25 July 2007, in final form 11 April 2008)

### ABSTRACT

An optical turbulence algorithm has been running operationally since April 2005 at the Mauna Kea Weather Center. The algorithm makes use of information on turbulence kinetic energy provided by a planetary boundary layer scheme available in the Pennsylvania State University–NCAR Mesoscale Model and estimates the turbulent fluctuations of the atmospheric refractive index and *seeing* over the summit area of Mauna Kea. To investigate the potential and limitations of the optical turbulence algorithm, one year of observed seeing data from four observatories is compared with the model forecast seeing and a statistical analysis is carried out. Sensitivity tests regarding the accuracy of the underlying numerical weather forecasts and the model's eddy diffusivity scheme are performed. Results from a simple calibration of the optical turbulence algorithm are presented.

### 1. Introduction

The fifth-generation Pennsylvania State University–National Center for Atmospheric Research Mesoscale Model (MM5) has been used to provide guidance for short-term weather forecasts at the Mauna Kea Weather Center (MKWC; see online at <http://mkwc.ifa.hawaii.edu>) since 1999 (Businger et al. 2002). Since April 2005, an optical turbulence algorithm has been running operationally (Cherubini et al. 2008). The implemented algorithm uses the information on turbulent kinetic energy (TKE) and temperature turbulent fluxes calculated in the Gayno–Seaman boundary layer scheme in MM5 (Gayno 1994; Shafran et al. 2000), and provides an estimate of the optical turbulent fluctuations of the atmospheric refractive index,  $C_n^2$ , and *seeing*. These parameters, which describe the optical turbulent state of the atmosphere, are widely used by astronomers in making and planning their observations. Since different turbulence conditions suit different types of observations, numerical forecasts of atmo-

spheric turbulence serve as guidance to schedule telescope usage. In addition they are used to optimize adaptive optics (AO), thus helping to reduce image degradation.

The horizontal resolution of MM5 over the summit of Mauna Kea is 1 km and the resolution is density weighted, with finer grid spacing near the ground ( $\sim$ tenths of a meter) and increasing to the order of  $\sim$ 1 km from the tropopause to the top of the model, fixed at 10 mb ( $\sim$ 25 km). For a more complete description of the MKWC forecasting system and the optical turbulence algorithm, please refer to Cherubini et al. (2006, 2008).

The implemented algorithm has been tested in selected case studies for which the observed vertical distribution of turbulence over Mauna Kea was available (Cherubini et al. 2008). Overall, the algorithm was able to reproduce the average behavior of the observed  $C_n^2$ , particularly in the low and midtroposphere. For the cases studied, the predicted and observed average values of seeing were reasonably well correlated. However, the observed data showed a temporal variability that the model was unable to capture, particularly at the highest levels where model vertical resolution degrades. Vertical profiles of  $C_n^2$ , for these cases, show discrepancies at some levels. Nevertheless, the average modeled and observed  $C_n^2$  profiles for the period of the site monitoring campaign show reasonable correspondence (Cherubini et al. 2008) (e.g., Fig. 1).

\* School of Ocean and Earth Science and Technology Contribution Number 7576.

*Corresponding author address:* Dr. Tiziana Cherubini, Department of Meteorology, University of Hawaii at Manoa, 2525 Correa Rd., Honolulu, HI 96825.  
E-mail: tiziana@hawaii.edu

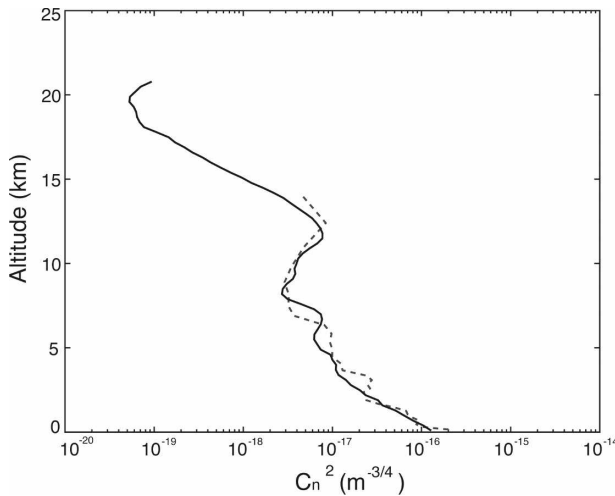


FIG. 1. Average  $C_n^2$  profiles from the 2002 Mauna Kea site monitoring campaign (black solid line) and from the MM5 data (dashed line).

The goal of the research presented in this paper is to use the observational datasets available at the summit of Mauna Kea to improve our understanding of the limits and the potential of the optical turbulence algorithm to provide accurate guidance for MKWC forecasters. To this end, observations from various Mauna Kea observatories were analyzed to understand the average diurnal and annual behavior of seeing. A year of MM5 simulated seeing output was used in comparisons and statistical analyses. Since a poor seeing prediction might be the consequence of a poor model forecast rather than a deficiency in the seeing algorithm, sensitivity tests regarding the accuracy of the underlying numerical weather forecasts were performed. Finally, a refinement of the optical turbulence algorithm was obtained by calibrating the diffusivity scheme involved in the calculation of  $C_n^2$  and seeing.

## 2. Data resources

The MKWC routinely collects seeing data as measured or estimated by several of the observatories located at the Mauna Kea summit. In general the summit observatories provide seeing data whenever there are favorable observing conditions. Telescope seeing is an estimation of the full-width half-maximum (FWHM) value based on the stellar image size, and it is defined, for an observation at zenith, by the following equation:

$$\phi = 0.98 \frac{\lambda}{r_0}, \quad (1)$$

where  $\lambda = 0.5 \mu\text{m}$  is chosen as a representative wavelength for optical astronomy and the Fried number  $r_0$  is

TABLE 1. Seeing data availability.\*

Provider	Instrument	Availability	Data frequency
CFHT	MegaPrime, MegaCam, WirCam	Feb 2005–present	3 min
Subaru	DIMM	Jun 2005–present	10 s
Subaru	Subset from the telescope auto-guider	Jun 2005–present	2–3 h
UKIRT	Cassegrain, WFCAM	Jan 2004–present	5 min
UH88	DIMM	Jun 2005–Jul 2006	70 s

\* For additional information see <http://www.cfht.hawaii.edu/Instruments/Imaging/> and <http://www.jach.hawaii.edu/UKIRT/instruments/wfcam/>.

obtained by vertical integration of the refractive index structure coefficient  $C_n^2$  along the optical path  $L$ :

$$r_0 = \left[ 0.423 \left( \frac{2\pi}{\lambda} \right)^2 \int_0^L C_n^2(z) dz \right]^{-3/5}. \quad (2)$$

A Differential Image Motion Monitor (DIMM) is a widely used instrument that estimates the Fried parameter, and astronomical seeing, by measuring the variance of the differential image motion in two small apertures cut out of a mask and applied to a telescope pupil (Tokovinin 2002; Sarazin and Roddier 1990). The measurement of the wave front slope difference over the two apertures is a form of wavefront curvature sensor that has the advantage of being substantially insensitive to tracking errors. Possible instrument biases and the effect of turbulence outer scale are discussed in Tokovinin (2002).<sup>1</sup>

Data providers are listed in Table 1 and include (i) the Canada–France–Hawaii Telescope (CFHT), which estimates seeing via the imaging instrument mounted on the telescope [MegaPrime, MegaCam, or wide-field-of-view infrared camera (WirCam)], (ii) the Subaru telescope, which measures seeing through a DIMM monitor mounted on the telescope catwalk (Uraguchi et al. 2006) and also provides a subset of the telescope estimated seeing, and (iii) the U.K. Infrared Telescope (UKIRT), which estimates seeing via either Cassegrain or infrared Wide-Field Camera (WFCAM) (Casali et al. 2007).

<sup>1</sup> The von Kármán turbulence model (Borgnino 1990; Ziad et al. 2000) introduces the spatial coherence wave front outer scale  $L_0$  (not to be confused with the geophysical local turbulence outer scale) to better describe the wave front statistics at scales of a few meters than the std Kolmogorov model (Roddier 1981), for which  $L_0 = \infty$ . Typical values for  $L_0$  are on the order of 20 m.

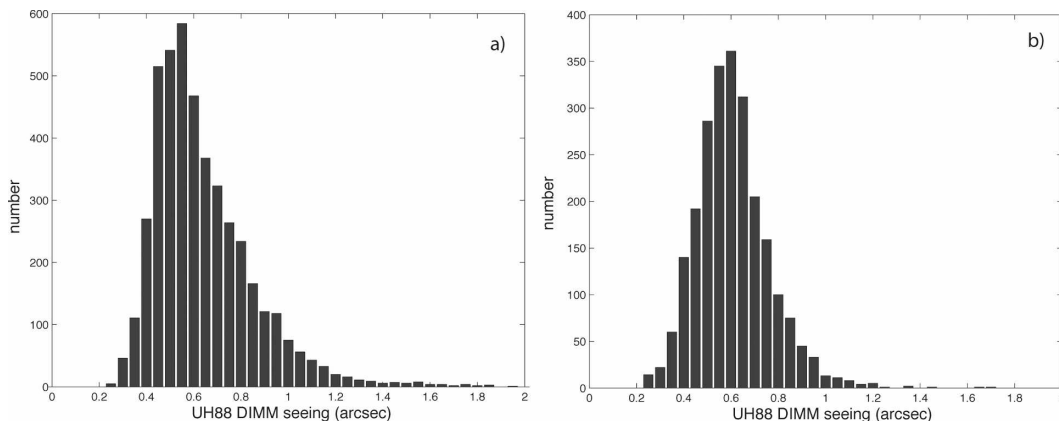


FIG. 2. Histograms of the distribution of seeing data from the UH88 DIMM monitor binned every 0.05 arc s for the month of (a) August 2005 and (b) May 2006.

Summit seeing data are also available for the period from June 2005 to July 2006 from a DIMM monitor that was temporarily installed at the University of Hawaii at Manoa 88-in. (UH88) telescope facility as a part of a summit monitoring campaign.

The DIMM at the Subaru telescope, mounted outside the telescope catwalk, operates in the open air at 12 m from the ground and 2.5 m from the telescope enclosure. The system automatically chooses different exposure times depending on the observing conditions so as to minimize the infinite exposure effect. The systematic bias that originates from finite exposure time has been estimated to be less than 2%, using the interlaced exposure correction method. The data are made available to the MKWC with a 10-s frequency. Given the high variability of the signal at this sampling frequency, a 5-min running average was applied to the data.

The UH DIMM consists of a 10 s Meade telescope with a two-aperture plate covering the front of the telescope. The two apertures are 5.9 mm in diameter and have a center-to-center separation of 19.4 mm. One of the apertures has a wedged plate that offsets the image formed from this aperture from the other. An SBIG ST-5 Charged-Coupled Device (CCD) camera with modified firmware takes interlaced exposures of 5 and 10 ms. The interlaced exposures are used to extrapolate the measured  $r_0$  to an effective 0-ms integration time. Its reported  $r_0$  is for this effective 0-ms integration and at a wavelength of 0.5  $\mu\text{m}$ . The DIMM is set up on the roof of the Coude' building of the UH 2.2-m telescope on the east ridge of the summit of Mauna Kea. The location is approximately 13 m above ground and about 7 m south of the 2.2-m telescope enclosure. The system is operated by a technician who sets up and performs the initial pointing of the telescope. The DIMM is lim-

ited to low wind speeds (<20 kt) because of severe vibrations of the telescope mount under larger wind conditions. The DIMM does not distinguish where turbulence is located and to first order is equally sensitive to all heights, although there is a second-order effect on scintillation that affects sensitivity at high altitudes. The location of the UH DIMM at about 13 m from the ground allows the instrument to be away from the greatest surface layer impact.

### 3. Results from observational data analysis

A good starting point for understanding seeing prediction at the summit of Mauna Kea is to use the observational data to learn more about the nature of seeing at this location. Figure 2 shows that a greater number of seeing observations was made during the month of August than during May 2002 and that the August seeing values were lower on average than those recorded during May. Figure 3 shows improved seeing (i.e., lower values) during the middle of the night when more observations are made. The MKWC will continue to refine the climatology of seeing as more data become available.

To compare the datasets, which differ because of the collection times and frequency, hourly averages were calculated. The cross comparison is limited to the time frame from June 2005 to the end of July 2006 when DIMM data were collected at the UH88. Quartiles for pairs of simultaneous observations (Table 2) and scatterplots comparing pairs of seeing datasets show that differences among different providers are not negligible (Fig. 4).

Differences between DIMM and large-size telescope seeing are expected, especially in the infrared range, where turbulence does not entirely conform to the stan-

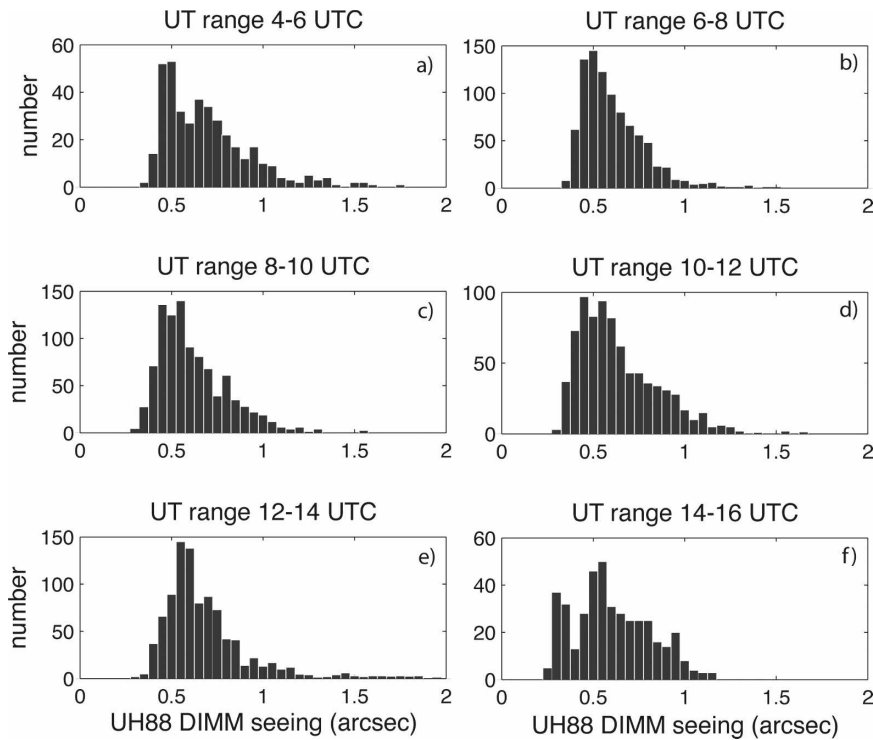


FIG. 3. (a)–(f) Histograms of seeing data from the UH88 DIMM monitor for the month of August 2005 every 2 h during the night.

standard infinite-scale model (Roddier 1981) and the effects of the turbulence outer scale should be considered (Tokovinin 2002). Also, the DIMM open-air measurements will differ from the telescope estimated seeing because of the effect of the dome and primary mirrors on turbulence. Finally, different locations on the summit with respect to local topography and surrounding buildings contribute to the observed discrepancies. For example, under conditions of easterly winds, particularly when the wind speeds increase above a certain threshold, it has been observed that the Subaru DIMM instrument consistently measures higher values of seeing (i.e., associated with more turbulence) than is reported by other instruments. This discrepancy can likely be attributed to its location on the west side of the telescope dome.

**4. Predicted versus observed seeing**

At the MKWC, the MM5 model is run 2 times per day. One model run is initialized at 0000 UTC [1400

Hawaiian standard time (HST)] and the second uses the 1200 UTC (0200 HST) initial conditions. Both runs provide a 60-h forecast. In this study only the data from the run initialized at 0000 UTC are used. When analyzing the data for a given night at the summit, say from 0600 (2000 HST) to 1600 UTC (0600 HST), the 6th to the 16th hour of the MM5 forecast is considered.

The model calculates seeing at each model level, and seeing values are available at every time step (i.e., every 3 s). Hourly averages of predicted seeing on the lowest model level (14 m above the ground), which is  $C_n^2$  integrated from that level to the model top, are used to compare with observed data (Fig. 5). Significantly, in all cases the distribution of points exhibits a funnel-like shape along the bisectrix—evidence that the forecast is more accurate during nights characterized by good observing conditions (i.e., low seeing values), which is exactly the time that the model guidance is most important for astronomers. The model-predicted seeing overestimates the observed seeing for all datasets, except for the one from Subaru (see biases in Table 3). Because of the instrument location, seeing data from Subaru’s DIMM tend to overestimate observed seeing values, particularly under conditions of moderate to strong easterly winds. As a consequence, some of the scatter in the plots of the predicted versus the observed value of seeing (Fig. 5) can be explained by the rela-

TABLE 2. Quartiles of the UH simultaneous observations.

	CFHT vs UH		Subaru vs UH		UKIRT vs UH		
Quartiles	25	0.65	0.60	0.72	0.57	0.47	0.58
	50	0.76	0.70	0.89	0.67	0.65	0.67
	75	0.91	0.85	0.91	0.85	0.81	0.89

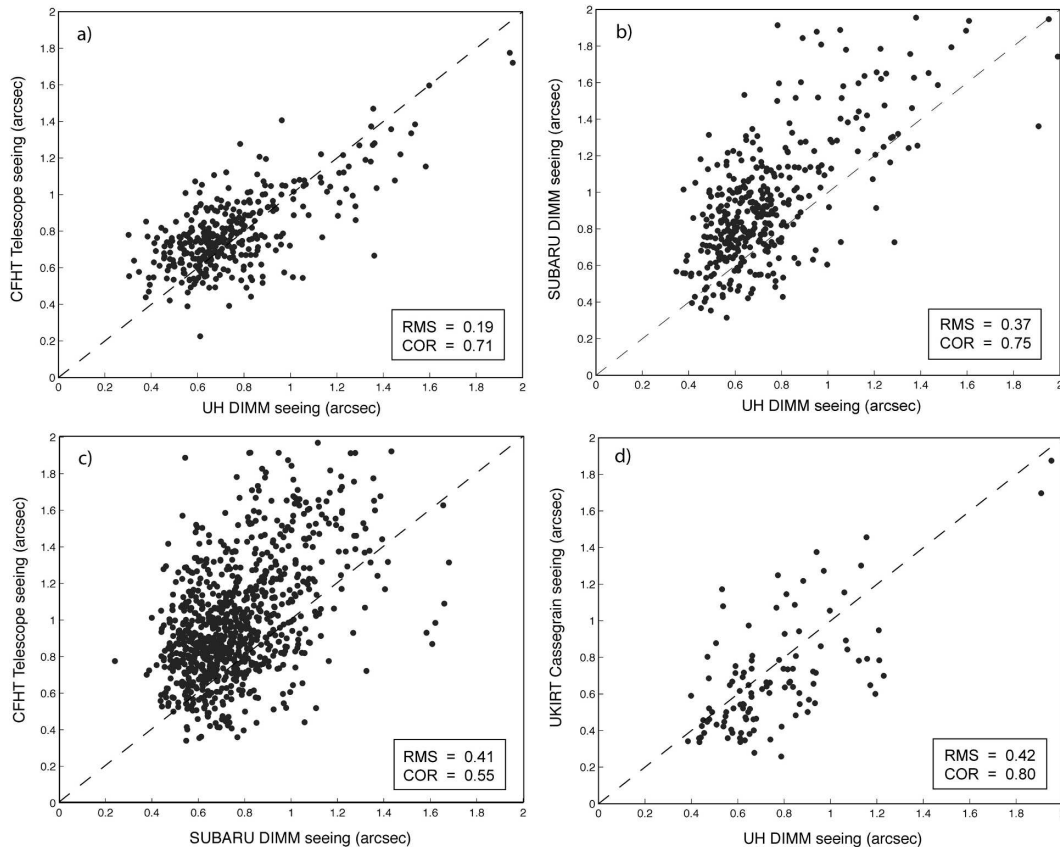


FIG. 4. Scatterplots of observed seeing: (a) CFHT telescope estimated seeing vs UH88 DIMM seeing, (b) Subaru DIMM vs UH88 DIMM seeing, (c) CFHT telescope estimated seeing vs Subaru DIMM seeing, (d) UKIRT Cassegrain estimated seeing vs UH-88 DIMM seeing. RMS and correlation coefficient (COR) are indicated in each plot.

tively low correlation found among measurements of seeing at the various sites (Fig. 4).

To determine whether poor seeing predictions were a consequence of a poor model weather forecast rather than a deficiency in the seeing algorithm, the accuracy of the weather forecasts was evaluated. Observations of temperature, relative humidity, and wind speed and direction are provided to the MKWC from weather sensors operated by several of the observatories. In this study summit weather observations provided by CFHT, UKIRT, and UH observatories were used. CFHT has sensors mounted on a standard 10-m weather tower, while UKIRT and UH operate sensors mounted on the roof of their building, at a height of  $\sim 10$  m from the ground and  $\sim 1$  m from the roof. The location of other observatories, with respect to the summit, and the local topography introduces biases in the comparison with model data. Therefore, weather observations collected by these other observatories were not included in this study. The mean values of hourly averaged time series from CFHT, UKIRT, and UH weather sensors were

calculated and treated as representative of the summit area to compare with the model-predicted values.

Analysis shows that the model generally performs well in terms of weather prediction at the summit level (Fig. 6). Errors in the forecasts coincide with periods of bad weather (i.e., unfavorable observing conditions). A notoriously bad spell of weather occurred from the middle of February to the beginning of April 2006, when a series of weather disturbances dominated the entire central Pacific area and the Hawaiian Islands. During this period, the model forecast slightly underestimated moisture and wind speed at the summit level.

The following cross analysis was carried out to quantify the effect of a low-accuracy forecast on the corresponding seeing forecast. A forecast event is first flagged as a “bad forecast” when one or more of the following conditions is verified: the model temperature absolute error is greater than  $2^{\circ}\text{C}$ ; the model relative humidity absolute error is greater than 20%; and the model wind absolute error is greater than 10 mph. The statistical sample, composed of the forecast and ob-

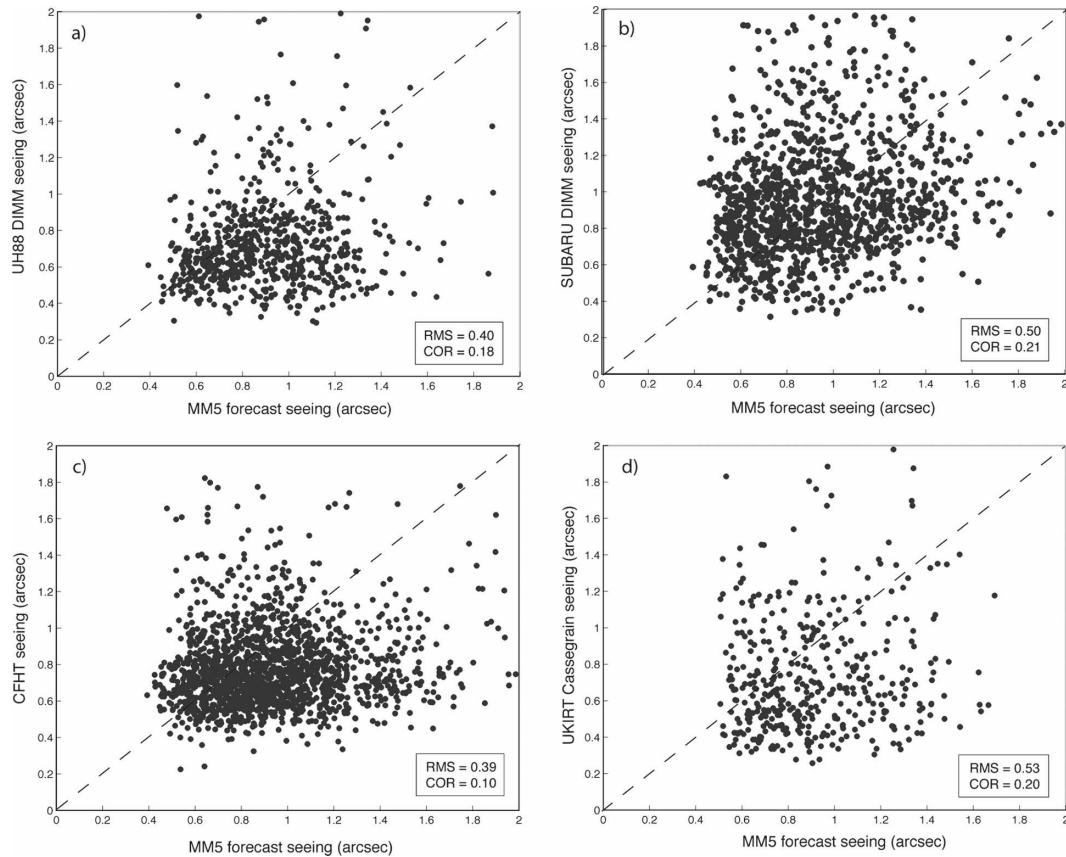


FIG. 5. Scatterplots of predicted vs observed seeing: (a) MM5 vs UH88 DIMM seeing; (b) MM5 vs Subaru DIMM seeing; (c) MM5 vs CFHT telescope estimated seeing; and (d) MM5 vs UKIRT Cassegrain estimated seeing. RMS and correlation coefficient are indicated within each plot.

served seeing pairs, was filtered out of those events for which a bad forecast flag was detected. The RMS and correlation coefficients were then recalculated for the forecast seeing when compared to the observed seeing. The statistics do not show sensitivity to the model errors, suggesting that when observations are carried out, summit-level weather parameters are on average well predicted by the model. The result from this basic analysis is not too surprising when one considers that model forecast errors increase during periods of bad weather when conditions are unfavorable for observing. A more complete analysis requires the comparison of modeled and observed Richardson numbers at vari-

ous levels for which profiles of winds and potential temperature are needed (Andreas et al. 2003). An ongoing field campaign and site characterization surveys will provide these data, which will be analyzed in future studies.

## 5. Tuning the algorithm

In this section a method is described for tuning the seeing algorithm to account for the impact of eddy diffusivity on the surface layer. The vertical distribution of turbulence over Mauna Kea was measured as a part of a site characterization campaign held during October and December 2002. Generalized Scintillation Detection and Ranging (G-SCIDAR; Vernin and Roddier 1973; Avila et al. 1997) and Multiaperture Scintillation Sensor (MASS; Kornilov et al. 2003) instruments operated during several nights then. The surface layer is transparent to MASS, and the G-SCIDAR data were only available above 70 m from the surface. Therefore, it was not possible to ascertain the performance of the seeing algorithm near the surface in Cherubini et al.

TABLE 3. Biases of the predicted vs observed seeing distribution.

	Bias (mean error)
MM5-UH88	0.17
MM5-Subaru	-0.07
MM5-CFHT	0.16
MM5-Cassegrain	0.13

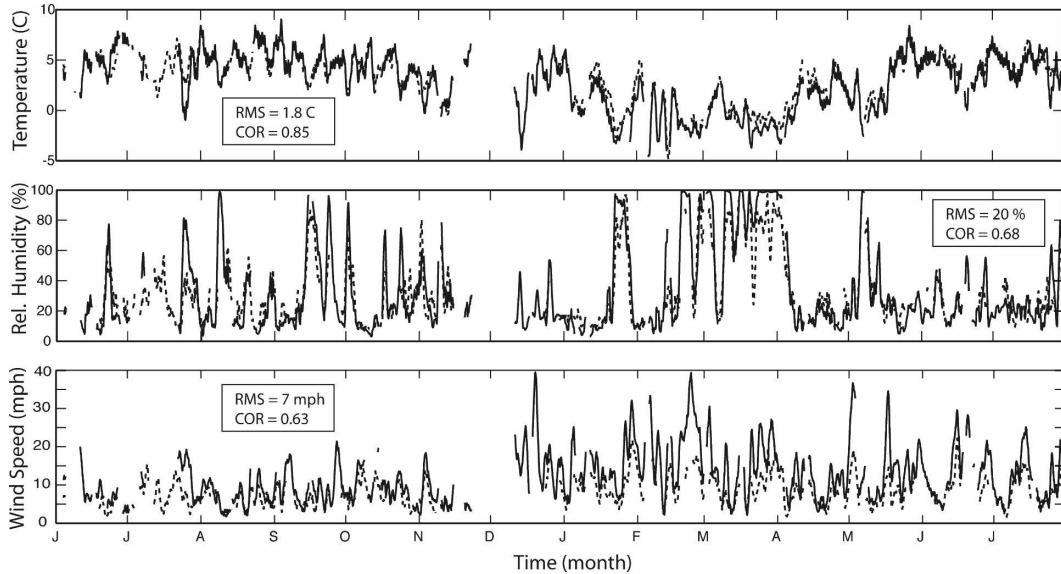


FIG. 6. Hourly averaged weather variables observed at the summit (solid line) and predicted by the MM5 (shaded line). RMSs and correlation coefficients are shown within each plot.

(2008). Output from daily model seeing forecasts consistently shows a rapid increase in predicted seeing through the lowest model levels (Fig. 7). This gradient in predicted seeing is consistent with a steep gradient in the profiles for  $C_n^2$  in the surface layer, and can be attributed to the impact of friction-induced turbulence (e.g., Fig. 8 inset).

In dealing with the nonlinear effects of turbulence in the surface layer, the relationship between surface energy exchange and the gradient in the direction normal to the surface of a conservative quantity, such as po-

tential temperature, has been extensively studied (Deardorff 1972; Troen and Mahrt 1986; Holtslag and Moeng 1991). This relationship can conveniently be parameterized by a correlation coefficient called the *diffusivity*. In the case of potential temperature, the thermal diffusivity is the ratio of the flux of heat through a specified surface by turbulence to the gradient of the mean potential temperature normal to that surface. In the planetary boundary layer (PBL) scheme used in the current operational MM5 configuration the thermal diffusivity is  $K_\theta$ :

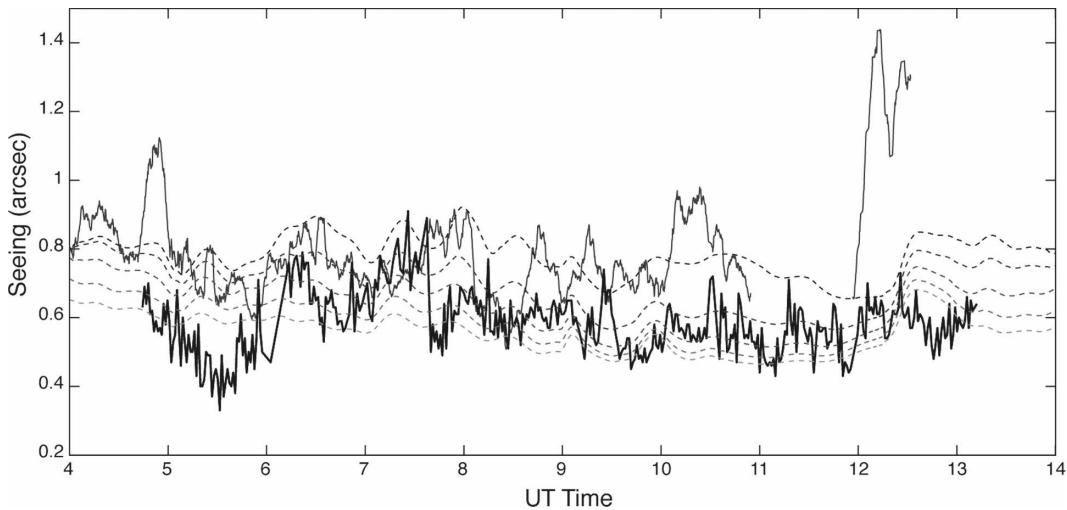


FIG. 7. Time series of seeing for the night of 12 May 2006 as measured by the Subaru DIMM (red solid line) and the UH88 DIMM (blue solid line), and predicted by the MM5 for the five lowest model levels (gray dashed lines).

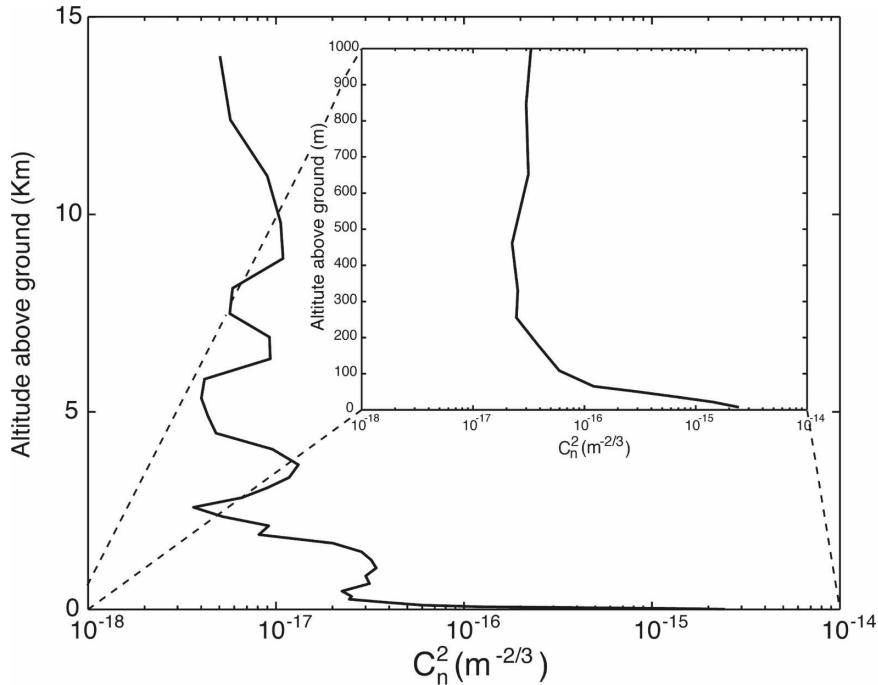


FIG. 8. MM5  $C_n^2$  profile valid at 0900 UTC 16 May 2006. The first kilometer above the ground is magnified in the inner window.

$$K_{\vartheta} = -2\omega'\vartheta' = L_h\sqrt{\text{TKE}}, \quad (3)$$

where TKE is the turbulent kinetic energy and  $L_h$  is the mixing length scale for heat. The TKE is a model prognostic variable, whereas  $L_h$  is calculated as a complex function of the TKE, basic mixing length scale, shear, and buoyancy (Ballard et al. 1991; Cherubini et al. 2008). The PBL scheme restricts values for diffusivity at the lowest model levels by a coefficient,  $K_{\text{ZOGS}}$ , multiplied by the ratio of  $L_h$  and the mixing length for momentum,  $L_m$ :

$$K_{\vartheta} = \max\left(K_{\vartheta}, \frac{L_h}{L_M} K_{\text{ZOGS}}\right), \quad (4)$$

where  $K_{\text{ZOGS}}$  is an empirical function of height (Fig. 9).

Specification of  $K_{\text{ZOGS}}$  influences the predicted gradients in  $C_n^2$  and in seeing in the lowest atmospheric levels. Although the default minimum value for vertical eddy diffusivity,  $K_{\text{ZOGS}}$ , is needed in the boundary layer scheme to insure numerical stability, it nevertheless holds a physical significance. In fact, within the MM5 model, the profile for the minimum value for eddy diffusivity over water differs from the one over land (profile 3 and CTRL, respectively, in Fig. 9). In essence, changes in  $K_{\text{ZOGS}}$  account for the impact of changes in the surface roughness on the model heat flux near the surface, under very stable conditions, which are the prevailing conditions during good observing

nights. Predicted seeing values for each night for the period June 2005 until the end of July 2006 were recalculated using various  $K_{\text{ZOGS}}$  profiles (Fig. 9) and the results were compared with observations taken by the UH88 DIMM (Fig. 10). This sensitivity analysis was

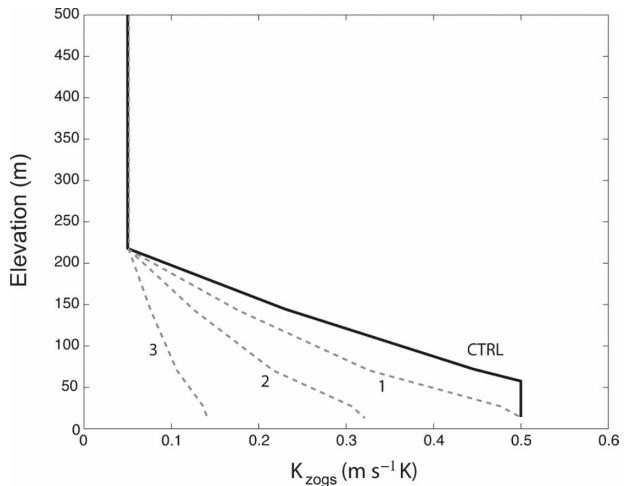


FIG. 9. Coefficient  $K_{\text{ZOGS}}$  plotted as a function of height near the surface. CTRL is the model default profile for  $K_{\text{ZOGS}}$  in the PBL scheme. Dashed lines labeled 1, 2, 3 are variations of the  $K_{\text{ZOGS}}$  profile applied in the sensitivity analysis, with profile 3 being the model default profile for the minimum of eddy diffusivity over water.



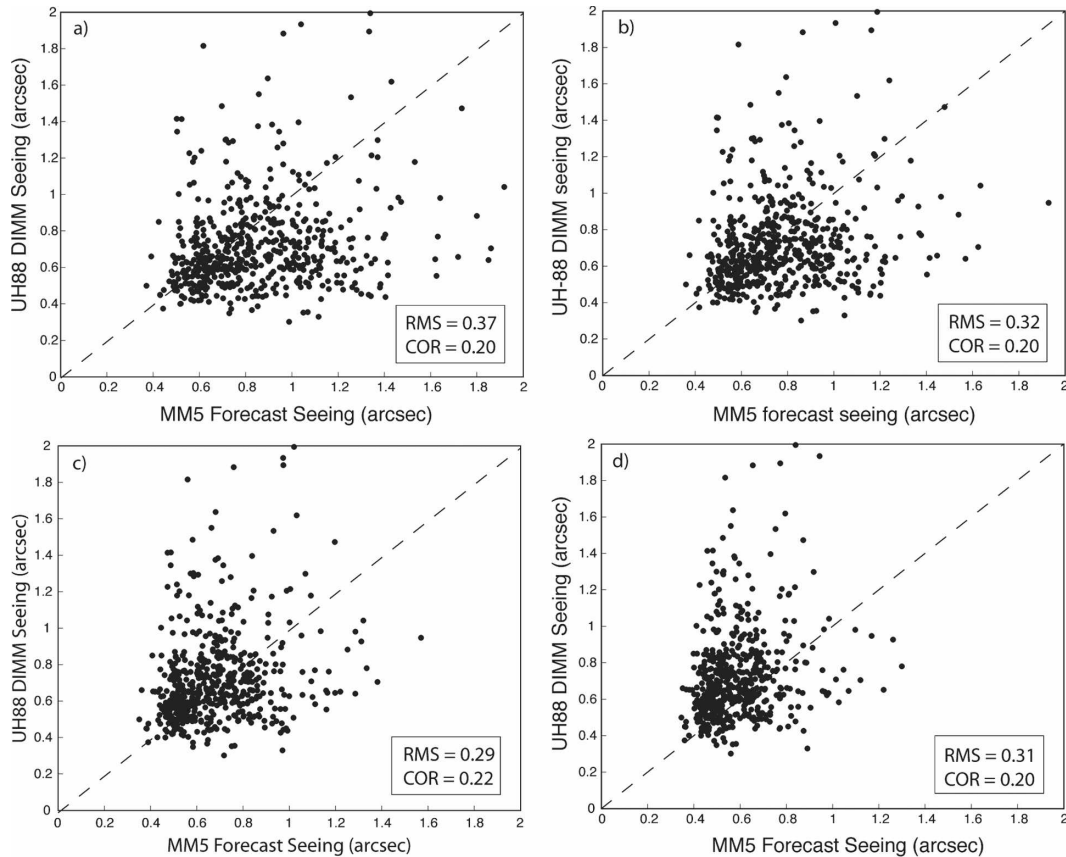


FIG. 10. MM5 vs UH88 DIMM seeing when (a) the default profile for  $K_{ZOGS}$  is used, (b) profile 1 for  $K_{ZOGS}$  is used, (c) profile 2 for  $K_{ZOGS}$  is used, and (d) profile 3 for  $K_{ZOGS}$  is used. Only nights with low wind shear aloft are included here.

carried out within the seeing algorithm, that is, without changing the profile for  $K_{ZOGS}$  in the model boundary layer parameterization, therefore not affecting the weather model predictions.

To isolate the contribution of surface turbulence from that due to turbulence aloft, the analysis was limited to nights with low shear, defined as those nights during which the difference in the horizontal wind between the 300- and 100-mb levels ( $\sim 10$  to 15 km above sea level) was less than 50 kt.

The UH88 DIMM seeing data were used to validate the model-predicted seeing. Experience suggests that the model-predicted seeing values are closer to measurements by a DIMM instrument than to estimates from an imaging instrument mounted on a telescope. Additional factors such as outer-scale influence and dome seeing affect the seeing estimation in a way that the algorithm is unable to model. Data from the Subaru DIMM show biases because of the location of the seeing monitor with respect to the summit terrain and the Subaru telescope dome, and therefore, are not used in this analysis.

Values of  $K_{ZOGS}$  corresponding to smaller values for the diffusion coefficient produce lower values of the predicted seeing (Fig. 10). Of all the profiles evaluated,  $K_{ZOGS}$  profile 2 results in the greatest reduction in scatter in the plot of the predicted versus observed seeing, which is reflected in the smallest RMS error and best correlation. In essence,  $K_{ZOGS}$  profile 2 best suits the environment on the summit area of Mauna Kea.

When all nights are included in the analysis and  $K_{ZOGS}$  profile 2 is applied, the RMS error is reduced (Fig. 11) but the correlation coefficient remains about the same, indicating a modest overall improvement in the algorithm performance when compared to the previous result without the calibration (Fig. 5a). Although the improvements in terms of correlation between the observed and predicted seeing values after the sensitivity analysis are small, the impact on the RMS ( $\sim 20\%$ ) is substantial for our operational applications, given that ideally the astronomers would like to see an RMS of 0.2 arc s. In practical terms, the importance of the guidance in decision making increases as the seeing improves, and it is during those times when the scatter in

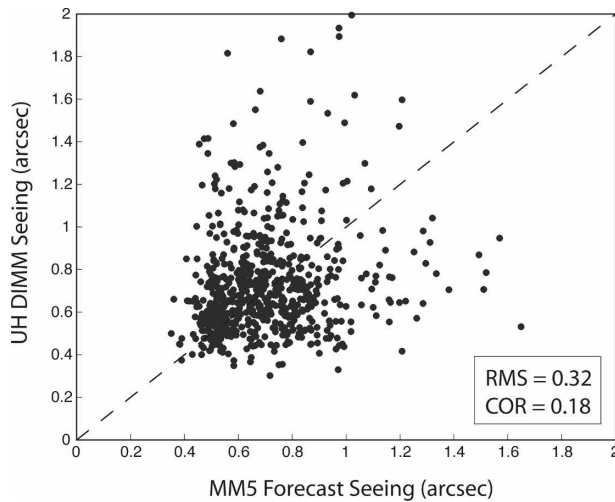


FIG. 11. MM5 vs UH88 DIMM seeing when the  $K_{ZOGS}$  profile 2 is used and all nights are included.

the model predictions is the least, making removal of any bias a significant step.

## 6. Conclusions and future work

In this paper, observational data collected on the summit of Mauna Kea are used in an effort to characterize the variation of seeing over the summit area and to validate an optical turbulence algorithm that has been implemented in the operational run of the MM5 model at the MKWC. The optical turbulence algorithm provides seeing predictions for the summit of Mauna Kea (Cherubini et al. 2008). Seeing observations or estimates made by several of the telescopes at the summit are routinely collected at the MKWC. These data have been used to first gain insight into the behavior of seeing over the summit. A comparison of seeing data from the different providers over a 14-month period reveals significant variation from site to site, making the task of model validation and calibration more challenging. The analysis shows that the algorithm performs best under good observing conditions and that the accuracy decreases for increasing values of the observed seeing.

To investigate the possibility that a poor seeing prediction could, in fact, be the result of a poor model forecast rather than a deficiency in the seeing algorithm, a sensitivity study of the seeing prediction to model weather forecast errors above the summit was carried out. The resulting seeing statistics showed very little sensitivity to model errors, which likely reflects the circumstance that significant model errors are most likely to occur under conditions of bad weather when the environment is unsuitable for making seeing obser-

ations. This result suggests that improvement in the optical turbulence algorithm can be achieved through algorithm refinement, rather than through improvement in the underlying model accuracy. To this end, the observed seeing datasets were used to tune the eddy diffusivity parameterization scheme involved in the calculation of  $C_n^2$  and therefore seeing. In reviewing the model output, it was noted that the algorithm consistently overestimated the gradients in  $C_n^2$  in the atmospheric layers nearest to the ground when compared to the observations. An analysis was undertaken of the sensitivity of predicted seeing values to changes in the parameter that regulates the model eddy diffusivity,  $K_{ZOGS}$ , in the lowest atmospheric layers. The minimum profile for the eddy diffusivity,  $K_{ZOGS}$ , is in fact often invoked, because during a typical observing night at the summit, the prevailing conditions are generally stable. To focus the analysis on the contribution of surface-induced turbulence on seeing, only nights during which the average shear aloft was weak were included. The model default minimum for the eddy diffusivity has been identified as a source of bias in the turbulence algorithm output. The density distribution of the predicted versus the observed seeing is, in fact, sensitive to changes in  $K_{ZOGS}$ . The analysis identified the value for  $K_{ZOGS}$  in the eddy diffusivity scheme that produced the best seeing prediction, and that value has subsequently been incorporated into the operational version of the optical turbulence algorithm.

The initial calibration of the optical turbulence algorithm described in this paper constitutes a viable first step toward tuning and improving the seeing model prediction, however, it will not be the last one. As the dataset of observed vertical profiles of  $C_n^2$  grows, it will provide an opportunity to further refine the algorithm. Similarly, as the archive of seeing data expands, the MKWC will be able to gradually construct a more complete climatology of seeing over Mauna Kea. At the time of this writing, a fixed  $C_n^2$ /seeing monitor is being installed at the summit of Mauna Kea. Additionally, data from a slope detection and ranging (SLODAR) profiler, an instrument able to accurately measure optical turbulence in the lowest atmospheric layers, will also be made available to the MKWC. Further algorithm validation and refinement will be performed when data from these new instruments become routinely available. Our analysis has drawn attention to one of the limitations of the turbulence algorithm. Future studies, with access to more robust turbulence data over the summit, will allow a more sophisticated approach to investigating the limitations, including investigating new parameterization schemes for turbulence within the model.

In the future, as computational resources expand, studies of the sensitivity of the algorithm performance to the horizontal and vertical resolution of the model will be undertaken. Numerical instabilities in the model associated with the interaction of atmospheric flow with complex topography will also be investigated.

*Acknowledgments.* We thank the following people for generously providing access to their weather and/or seeing data: Mark Chun (UH88), Fumihiro Uraguchi (Subaru), Jim Thomas (CFHT), and Tom Kerr (UKIRT). The National Astronomical Observatory of Japan provides computer resources for the MM5 simulations that are run at the Subaru telescope facility in Hilo, Hawaii.

#### REFERENCES

- Andreas, E. L., C. W. Fairall, P. O. G. Persson, and P. S. Guest, 2003: Probability distributions for the inner scale and the refractive index structure parameter and their implications for flux averaging. *J. Appl. Meteor.*, **42**, 1316–1329.
- Avila, R., J. Vernin, and E. Masciadri, 1997: Whole atmosphere turbulence profiling with generalized G-SCIDAR. *Appl. Opt.*, **36**, 7898–7905.
- Ballard, S. P., B. W. Golding, and R. N. B. Smith, 1991: Mesoscale model experimental forecasts of the haar of northeast Scotland. *Mon. Wea. Rev.*, **119**, 2107–2123.
- Borgnino, J., 1990: Estimation of the spatial coherence outer scale relevant to long base-line interferometry and imaging in optical astronomy. *Appl. Opt.*, **29**, 1863–1865.
- Businger, S., R. McLaren, R. Ogasawara, D. Simons, and R. J. Wainscoat, 2002: Starcasting. *Bull. Amer. Meteor. Soc.*, **83**, 858–871.
- Casali, M., and Coauthors, 2007: The UKIRT wide-field camera. *Astron. Astrophys.*, **467**, 777–784.
- Cherubini, T., S. Businger, C. Velden, and R. Ogasawara, 2006: The impact of satellite-derived atmospheric motion vectors on mesoscale forecasts over Hawaii. *Mon. Wea. Rev.*, **134**, 2009–2020.
- , —, R. Lyman, and M. Chun, 2008: Modeling optical turbulence and seeing over Mauna Kea. *J. Appl. Meteor. Climatol.*, **47**, 1140–1155.
- Deardorff, J. W., 1972: Theoretical expression for the countergradient vertical heat flux. *J. Geophys. Res.*, **77**, 5900–5904.
- Gayno, G. A., 1994: Development of a higher-order, fog-producing boundary layer model suitable for use in numerical weather prediction. M.S. thesis, Department of Meteorology, The Pennsylvania State University, 104 pp.
- Holtslag, A. A. M., and C.-H. Moeng, 1991: Eddy diffusivity and countergradient transport in the convective atmospheric boundary layer. *J. Atmos. Sci.*, **48**, 1690–1698.
- Kornilov, V., A. A. Tokovinin, O. Voziakova, A. Zaitsev, N. Shatsky, S. F. Potanin, and M. S. Sarazin, 2003: Mass: A monitor of the vertical turbulence distribution. *Adaptive Optical System Technologies II*, P. L. Wizinowich and D. Bonaccini, Eds., International Society for Optical Engineering (SPIE Proceedings, Vol. 4839), 837–845.
- Roddier, F., 1981: The effect of atmospheric turbulence in optical astronomy. *Prog. Opt.*, **19**, 281–377.
- Sarazin, M., and F. Roddier, 1990: The ESO differential image motion monitor. *Astron. Astrophys.*, **227**, 294–300.
- Shafraan, P. C., N. L. Seaman, and G. A. Gayno, 2000: Evaluation of numerical predictions of boundary layer structure during the Lake Michigan ozone study. *J. Appl. Meteor.*, **39**, 412–426.
- Tokovinin, A., 2002: From differential image motion to seeing. *Publ. Astron. Soc. Pac.*, **114**, 1156–1166.
- Troen, I., and L. Mahrt, 1986: A simple model of the atmospheric boundary layer: Sensitivity to surface evaporation. *Bound.-Layer Meteor.*, **37**, 129–148.
- Uraguchi, F., N. Takato, A. Miyashita, and T. Usuda, 2006: The DIMM station at Subaru Telescope. *Ground-based and Airborne Telescopes*, L. M. Stepp, Ed., International Society for Optical Engineering (SPIE Proceedings, Vol. 6267), 62670N, doi:10.1117/12.671798.
- Vernin, J., and F. Roddier, 1973: Experimental determination of two-dimensional spatiotemporal power spectra stellar light scintillation. Evidence for a multiplayer structure of the air turbulence in the upper troposphere. *J. Opt. Soc. Amer.*, **63**, 270–273.
- Ziad, A., R. Conan, A. Tokovinin, F. Martin, and J. Borgnino, 2000: From the grating scale monitor to the generalized seeing monitor. *Appl. Opt.*, **39**, 5415–5425.